Mutual Inductance Identification of IPT System Based on Soft-Start Process

Lei Wang, Pan Sun, Xusheng Wu, Jin Cai, Qijun Deng, Jun Sun, and Hang Zhou

***Abstract*—Accurate estimation of mutual inductance in wireless power transfer (WPT) system is a prerequisite for accurate identification of load parameters, which is critical in system constant output and efficiency tracking control. In this article, a general load decoupling method for WPT system considering soft-start process and battery initial voltage is proposed. Moreover, a double-sided *LCC* topology is used to explain how to calculate the boundary conditions of load decoupling. Based on the proposed load decoupling method, a mutual inductance identification method is proposed for WPT system with double-sided *LCC* topology. Within the frequency range recommended, the unique solution of mutual inductance can be obtained by solving high-ordered equivalent impedance equation. In this case, there is no need to discuss the situation for multiple solutions. Based on the WPT prototype, the effectiveness of the proposed load decoupling method is verified, and parameter sensitivity of the identification method is analyzed in detail. Finally, the proposed method is experimentally verified. Results show that high identification accuracy can be achieved even when the coils are misaligned. Compared with the existing identification methods, the proposed method does not need any additional switches and auxiliary circuits, which reduces the complexity and system cost effectively.**

***Index Terms*—Coupling coefficient, load decoupling, mutual inductance parameter identification, parameter identification, wireless power transfer (WPT).**

NOMENCLATURE

$T_1 - T_4$	Primary-side MOSFETs.
$D_1 - D_4$	Secondary-side rectifier diodes.
$U_{\rm dc}$	DC input voltage.
$u_{\rm inv}$	Inverter output voltage.
$i_{\rm inv}$	Inverter output current.
$u_{\rm rec}$	Rectifier input voltage.
$i_{\rm rec}$	Rectifier input current.
$U_{\rm Bat}$	Battery voltage.
$I_{\rm Bat}$	Battery charging current.
L_p	Self-inductance of the transmitting coil.
L_s	Self-inductance of the receiving coil.
$U_{\rm dc\_set}$	Rated input dc voltage.
$U_{\rm inv\_f}$	Fundamental component of the inverter output voltage.
$U_{\rm inv\_f\_p}$	Fundamental component amplitude of the inverter output voltage.
$U_{\rm rec\_f\_p}$	Fundamental component amplitude of the rectifier input voltage.
$U_{\rm rec\_f\_p\_iden}$	Fundamental component amplitude of the rectifier input voltage during mutual inductance identification.
$U_{\rm Bat\_max}$	Battery charging cut-off voltage.
$U_{\rm Bat\_min}$	Battery discharge cut-off voltage.
$U_{\rm Bat\_initial}$	Battery initially voltage.
L_1	Primary-side compensation inductance.
C_1	Primary-side parallel compensation capacitor.
C_p	Primary-side series compensation capacitor.
L_2	Secondary-side compensation inductance.
C_2	Secondary-side parallel compensation capacitor.
C_s	Secondary-side series compensation capacitor.
M	Mutual inductance between the transmitting and receiving coils.
$M_{\rm iden}$	Identification value of mutual inductance.
R_{L1}	Stray resistance of L_1.
R_{Lp}	Ftray resistance of L_p.
R_{Ls}	Stray resistance of L_s.
R_{L2}	Stray resistance of L_2.
k	Coupling coefficient between the transmitting and receiving coils.
u_{c1}	Voltage on capacitor C_1.
i_p	Current on the transmitting coil.
U_{c1_mea}	Measured effective values of u_{c1}.
I_{p_mea}	Measured effective values of i_p.
$\omega_{o1} - \omega_{o4}$	Resonant angular frequency in different networks.
ω	Working angular frequency.
$\omega_{\rm iden}$	Working angular frequency during mutual inductance identification.
$f_{\rm iden}$	Working frequency during mutual inductance identification.
u_{c2}	Voltage on capacitor C_2.

Manuscript received September 27, 2021; revised December 28, 2021; accepted January 7, 2022. Date of publication January 13, 2022; date of current version February 18, 2022. This work was supported in part by National Natural Science Foundation of China under Grant 52007195 and in part by the Group Project in Hubei Province Natural Science Foundation of Innovation under Grant 2018CFA008. Recommended for publication by Associate Editor J. Acero. *(Corresponding authors: Pan Sun; Qijun Deng.)*

Lei Wang, Pan Sun, Xusheng Wu, Jin Cai, Jun Sun, and Hang Zhou are with the School of Electrical Engineering, Naval University of Engineering, Wuhan 430030, China (e-mail: 15198243251@163.com; chinasunpan@163.com; wuxusheng_hg@163.com; caijincj@126.com; 1292038814@qq.com; leochou_whu@163.com).

Qijun Deng is with the School of Electrical Engineering and Automation, Wuhan University, Wuhan 430072, China (e-mail: dqj@whu.edu.cn).

Color versions of one or more figures in this article are available at https://doi.org/10.1109/TPEL.2022.3142289.

Digital Object Identifier 10.1109/TPEL.2022.3142289

I. Introduction

WIRELESS power transfer (WPT) technology has been successfully applied to medical implantable devices [1], consumer electronics [3], unmanned aerial vehicles (UAVs) [4], underwater vehicles [5], and many other equipment. In recent years, its potential for electric vehicles (EVs) charging has been widely exploited, and relevant excellent research results have emerged [6], which proves its feasibility in wireless charging of EV. Compared with the traditional plug-in charging pile, electric vehicle wireless charging has the advantages of no physical contact, no electrical interconnection, and higher safety. However, for wireless charging, the transmission efficiency, constant output, and transmission power of the system are significantly affected by the magnetic coupling strength and the displacement between the coils [12]. Taking the wireless power supply for EVs as an example, different EVs have different power requirements and load characteristics, and the mutual inductance will change due to the different vertical heights and the alignment of chassis. Therefore, it is necessary to estimate the mutual inductance between coils, and the accurate mutual inductance identification is a prerequisite for an inductive wireless power transfer (IPT) system with constant output and high efficiency, which does not require a wireless communication system.

A variety of methods have been proposed to realize mutual inductance identification [14]. Jiwariyavej *et al.* [14] give a method for mutual inductance identification from the transmitting side under the premise of a known load condition. However, in practical situations, the load usually is unknown and variable. Chow *et al.* [15] establish differential equations for the series-series (SS) topology and obtain identification value of mutual inductance and load by solving fourth-order differential equations. However, the process of this method is very complicated, which is not suitable for WPT systems with composite topology compensation networks. In [16], a mutual inductance and load identification method for SS topology is proposed. This method is carried out under the assumption of a complete resistive rectify load, which has a limited range of application, such as SS topology. With the help of auxiliary circuit switching capacitors, [17] makes the system work in two operation modes. In these two modes, the binary equations are established respectively, and the identification values of the load and the mutual inductance are obtained by solving the equations. Although the principle of this method is simple and easy to understand, the identification procedure must be completed by adding auxiliary circuits, which increases the complexity and cost of the system. In [18], a load and mutual inductance identification method for wireless charging system based on the secondary side parallel compensation topology is proposed taking advantage of the particularity of the secondary side parallel compensation network. This method can be realized regardless of the compensation topology of the primary resonant circuit, and does not need other auxiliary circuits. In this case, cost and complexity of the system can be reduced. Zhao *et al.* [20] proposed a decoupling method between load and system by using buck–boost switch at the back end of rectifier bridge, so as to realize the identification of mutual inductance and load. This method needs to switch between mutual inductance identification mode and charging mode, which affects the charging performance. In the latest study in [21], load is decoupled by controlling a semiactive rectifier bridge, and a hardware based mutual inductance monitoring method is proposed for WPT system based on SS topology. This method analyzes the relationship between working frequency and equivalent input impedance and obtains the coupling coefficient through frequency scanning calculation.

Soft start is commonly required for the system to avoid device damage due to excessive voltage and current [22]. Shi *et al.* [22] describe a way to achieve soft-start of IPT systems by using the dc/dc converter at the front end of the inverter. This method regulates the inverter output voltage by changing duty cycle of the dc/dc to suppress inrush current and achieve soft-start. The advantage of this method is that the inverter can maintain zero voltage switch (ZVS) during soft-start process.

Another solution to change the output voltage of inverter is to adjust its pulsewidth or frequency. So far, based on changing the pulsewidth or frequency of the inverter, many different soft-start control strategies and system steady-state control strategies have been studied, which can be divided into the following three categories.

1) Variable pulsewidth control, including symmetrical pulsewidth control such as phase-shift (PS) control [23], and asymmetrical pulsewidth control such sociometrical duty-cycle control [24].
2) Variable frequency (VF) control [25]–[27].
3) Variable frequency phase shift (VFPS) control. Phase shift control is a basic way to change the inverter output voltage, but it the potential to make the inverter lose ZVS. In order to ensure the ZVS of the inverter, VFPS control is widely studied [28]–[30].

In fact, lots of information regarding the WPT system can be extracted from the soft-start process. Hence, a method of load decoupling and mutual inductance identification is proposed in this article based on the soft-start process.

The rest of this article is organized as follows. In Section II, the wireless charging technology based on WPT is described, and a general load decoupling method based on the initial voltage of battery and the soft start is proposed. In Section III, taking double-sided *LCC* topology as an example, an effective mutual inductance identification method is proposed based on the premise of load decoupling, and the calculation process of boundary conditions of load decoupling is explained in detail. In Section IV, based on the WPT system prototype and coil parameters, the parameter sensitivity of the algorithm is analyzed in detail. In Section V, the correctness and feasibility of the presented mutual inductance identification method are verified by simulation and experiment. Finally, Section VI concludes this article.

II. System's Overview and Load Decoupling Methods

A. Wireless Charging System Based on WPT

The wireless charging system based on WPT includes dc power supply module, high-frequency full-bridge inverter, coils and compensation networks, and an equivalent load module.

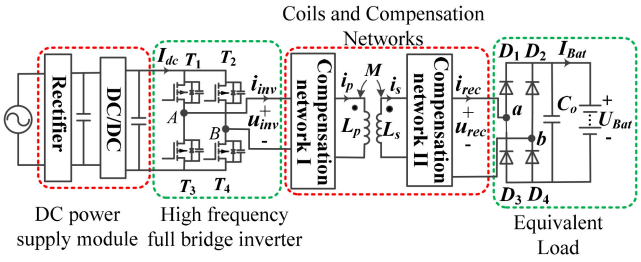

Fig. 1. WPT-based wireless charging system structure diagram.

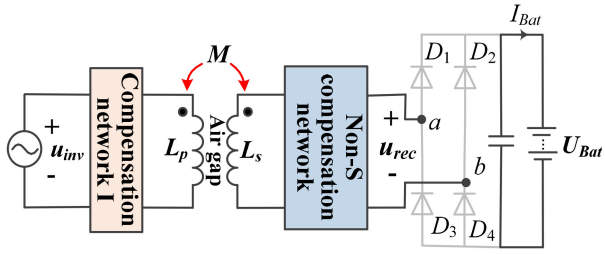

Fig. 2. Equivalent circuit when load is decoupled.

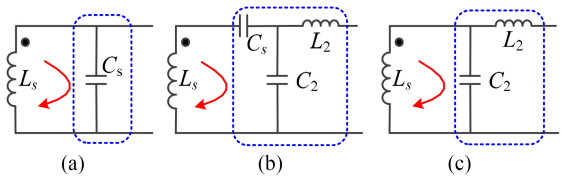

Fig. 3. (a) Parallel, (b) *LCC* compensation, and (c) *LCL* compensation in the secondary side.

Its structure is shown in Fig. 1. Among them, the dc power module provides dc input voltage $U_{\rm dc}$ for the WPT system. The high-frequency full-bridge inverter converts the dc input voltage $U_{\rm dc}$ into a high-frequency square wave voltage and sends it to the receiving coils and compensation networks. According to different transmission characteristics, the compensation networks have different kinds of topologies [31]. The rectifier composed of $D_1 - D_4$ rectifies the high frequency ac power from the compensation network into a stable dc output voltage for battery charging. In Fig. 1, L_p and L_s are the self-inductances of transmitting coil and receiving coil, respectively, while M is the mutual inductance between transmitting coil and receiving coil. $U_{\rm Bat}$ and $I_{\rm Bat}$ are the battery charging voltage and charging current, $U_{\rm dc}$ and $I_{\rm dc}$ are the dc input voltage and current, respectively. $u_{\rm inv}$ and $i_{\rm inv}$ are the inverter output voltage and current, respectively. $u_{\rm rec}$ and $i_{\rm rec}$ are the input voltage and current of equivalent load, respectively. It should be noted that low-cost uncontrollable diode is generally used to form a full-bridge rectifier. If bidirectional WPT is required, a fully controlled MOSFET is needed [32]. Since the bidirectional WPT is not within the scope of this study, the WPT system in this article adopts uncontrolled full bridge rectifier.

B. Load Decoupling Using Soft Start Process

Two common open-loop soft start methods are used as examples to illustrate how the start-up process can be used to achieve load decoupling and mutual inductance identification.

1) PS control. Keep the input dc voltage at the rated voltage $U_{\rm dc\_set}$, and control the conduction angle α of the inverter to slowly increase from zero to achieve soft start. According to [21], the relationship between the inverter conduction angle α and the fundamental component amplitude of the inverter output voltage $U_{\rm inv\_f\_p}$ at this time conforms to the following:

$$U_{\rm inv\_f\_p} = \frac{4}{\pi} U_{\rm dc\_set} \sin\left(\frac{\alpha}{2}\right). \tag{1}$$

2) Keep the conduction angle α at $\pi - \theta$ (θ is the dead time), and realize soft start by controlling the input dc voltage $U_{\rm dc}$ to slowly increase from zero. The relationship between $U_{\rm inv\_f\_p}$ and the dc input voltage $U_{\rm dc}$ conforms to the following:

$$U_{\rm inv\_f\_p} = \frac{4}{\pi} U_{\rm dc} \sin\left(\frac{\pi - \theta}{2}\right). \tag{2}$$

According to [33], the battery pack has corresponding charging and discharging cut-off voltages $U_{\rm Bat\_max}$ and $U_{\rm Bat\_min}$. Therefore, if the battery pack is ready to be charged, the initial battery voltage $U_{\rm Bat\_initial}$ is not zero and satisfies the following:

$$U_{\rm Bat\_initial} \geq U_{\rm Bat\_min}. \tag{3}$$

In summary, there must be a voltage interval $\Delta U_{\rm inv\_f\_p} = 0 \sim U'_{\rm inv\_f}$ during the soft-start process, in which $U_{\rm rec\_f\_p} < U_{\rm Bat\_min}$. In other words, the rectifier bridge is open in this voltage interval, and the battery load is decoupled from the system. When the load is decoupled, the equivalent circuit is shown in Fig. 2. The gray line in Fig. 2 indicates that the rectifier is open.

The battery discharge cut-off voltage $U_{\rm Bat\_min}$ is determined by the battery parameters, and it is known in the design process [35]. Therefore, (4) based on $U_{\rm Bat\_min}$ can be used as the voltage boundary condition for load decoupling, under which mutual inductance identification can be effectively performed

$$U_{\rm rec\_f\_p\_iden} < U_{\rm Bat\_min}. \tag{4}$$

In (4), $U_{\rm rec\_f\_p\_iden}$ represents the amplitude of the fundamental wave component of the voltage at the front end of the rectifier in the mutual inductance identification phase.

It is not difficult to understand that the WPT systems with nonseries compensation on the secondary side can use the above-mentioned load decoupling method for mutual inductance identification. Hence, the secondary side compensation network should be parallel, *LCC*, or *LCL* compensation network, as shown in Fig. 3.

In fact, most of the existing research achievements on the parameter identification of IPT systems are about SS topology. The research results of non-SS topology, however, are few. The load decoupling method proposed in this article is applicable to the IPT system with nonseries compensation on the secondary side, which provides more possibilities for the mutual inductance identification of IPT systems. The feasibility of the proposed mutual inductance identification method in other topologies has been proven. Due to the space limitation, this article only takes

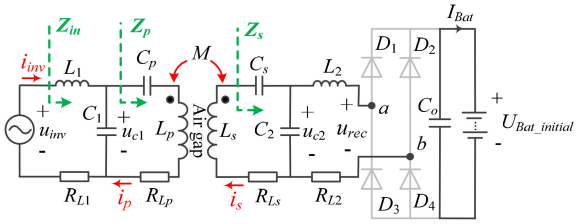

Fig. 4. Fundamental equivalent circuit and its components of WPT based on double-sided *LCC* compensation network.

the double-sided *LCC* topology as an example for illustration. The calculation method of the load decoupling boundary conditions and the realization of mutual inductance identification will be described in detail in Section III.

III. Proposed Mutual Inductance Identification Method

A. Principle of the Proposed Mutual Inductance Identification Method

Relevant analysis of this research is conducted on the WPT system with double-sided *LCC* compensation network, and its topology is shown in Fig. 4.

The compensation network is composed of L_1, C_1, C_p on the transmitting side and L_2, C_2, C_s on the receiving side. L_p, L_s, and M are self-inductances of transmit coil, receive coil, and mutual inductance between them, respectively. R_{L1}, R_{Lp}, R_{Ls}, and R_{L2} are the stray resistances of L_1, L_p, L_s, and L_2, respectively. $U_{\mathrm{Bat\_initial}}$ is the initial voltage of the battery to be charged.

According to [36], under the ideal condition, the circuit parameters are designed by (5) to realize constant current output characteristics of the topology at a constant ideal resonant frequency

$$\begin{cases} \omega_{o1}^2 = \frac{1}{L_1 C_1} \\ \omega_{o2}^2 = \frac{1}{L_2 C_2} \\ \omega_{o3}^2 = \frac{1}{(L_p - L_1) C_p} \\ \omega_{o4}^2 = \frac{1}{(L_s - L_2) C_s}. \end{cases} \tag{5}$$

In (5), $\omega_{o1}, \omega_{o2}, \omega_{o3}$, and ω_{o4} are the nominal resonant angular frequency, which are independent of coupling coefficient k and load conditions and only relevant to compensation network parameters of the system. Ideally, $\omega_{o1}, \omega_{o2}, \omega_{o3}$, and ω_{o4} should be almost identical, but in practical situation, there will be deviations between them due to the parameter shifts and soft switching requirement.

Under the rules in Section II-B, when $U_{\mathrm{inv\_}f\_p\_\mathrm{iden}}$ is used as the working voltage, the diode rectifier bridge will be open. In this case, the load and the system are decoupled. Then, according to the circuit principle

$$Z_s = R_{Ls} + j\left(\omega L_s - \frac{1}{\omega C_s} - \frac{1}{\omega C_2}\right) = R_s + jX_s \tag{6}$$

where ω is the working angular frequency of the system.

The reflection impedance can be expressed as follows:

$$Z_{sp} = \frac{(\omega M)^2}{Z_s} = \frac{(\omega M)^2 \cdot R_s}{R_s^2 + X_s^2} - j\frac{(\omega M)^2 \cdot X_s}{R_s^2 + X_s^2}. \tag{7}$$

Then, Z_p can be expressed by (8)

$$\begin{aligned} Z_p &= R_{Lp} + j\left(\omega L_p - \frac{1}{\omega C_p}\right) + Z_{sp} \\ &= R_{Lp} + jX_{Lp} + Z_{sp}. \end{aligned} \tag{8}$$

From (5), it can be seen that C_1 and L_1 constitute a resonant filter, so the harmonic components in i_p and u_{c1} are very low. Therefore, in order to reduce the identification error, the effective value of u_{c1} and i_p are measured to calculate the modulus of equivalent impedance Z_p. Combining (7) and (8) to establish (9)

$$\begin{aligned} |Z_p| &= \frac{U_{c1\_\mathrm{mea}}}{I_{p\_\mathrm{mea}}} \\ &= \sqrt{\left(\frac{(\omega M)^2 \cdot R_s}{R_s^2 + X_s^2} + R_{Lp}\right)^2 + \left(X_{Lp} - \frac{(\omega M)^2 \cdot X_s}{R_s^2 + X_s^2}\right)^2} \end{aligned} \tag{9}$$

where U_{c1_mea} and I_{p_mea} are the measured effective values of u_{c1} and i_p, respectively, $X_{Lp} = \omega L_p - 1/(\omega C_p)$.

Substituting the measured value U_{c1_mea} and I_{p_mea} into (9), and solving (9) to obtain the mutual inductance identification value M_{iden}.

Through analysis of (9), it can be seen that $|Z_p|$ is a function of mutual inductance M. Let $|Z_p| = y$, then $y = f(M)$. Equation (10) can be obtained by taking the derivative of (9)

$$\begin{aligned} \frac{\partial y}{\partial M} &= \frac{2\omega^2 M}{R_s^2 + X_s^2} \\ &\quad \cdot \frac{(\omega M)^2 + R_{Lp}R_s - X_{Lp}X_s}{\sqrt{\left(\frac{(\omega M)^2 \cdot R_s}{R_s^2 + X_s^2} + R_{Lp}\right)^2 + \left(X_{Lp} - \frac{(\omega M)^2 \cdot X_s}{R_s^2 + X_s^2}\right)^2}}. \end{aligned} \tag{10}$$

Let $\frac{\partial y}{\partial M} = 0$, the extremal points can be obtained as (11) shows

$$M_1 = 0, M_{2,3} = \pm\frac{1}{\omega}\sqrt{X_{Lp}X_s - R_{Lp}R_s}. \tag{11}$$

It can be seen from (11) that there are three extremal points. For $y = f(M)$, whether $M_{2,3}$ has a real solution depends on the value of $X_{Lp}X_s - R_{Lp}R_s$. The different situations of $X_{Lp}X_s - R_{Lp}R_s$ are discussed as follows.

According to (5), (6), and (8), $X_s = \omega L_s - \frac{1}{\omega C_s} - \frac{1}{\omega C_2}$, $X_p = \omega L_p - \frac{1}{\omega C_p} - \frac{1}{\omega C_1} = X_{Lp} - \frac{1}{\omega C_1}$, assuming that the natural resonant angular frequencies of $X_s = 0$, $X_p = 0$, and $X_{Lp} = 0$ are ω_{os}, ω_{op}, and ω_{Lp}, respectively, and then $\omega_{Lp} = \sqrt{\frac{1}{L_p C_p}}$, $\omega_{op} = \sqrt{\frac{C_p + C_1}{L_p C_p C_1}}$, and $\omega_{Lp} < \omega_{op} \approx \omega_{os}$. Based on the above conclusions, the following analysis can be obtained.

TABLE I
INFLUENCE OF DIFFERENT OPERATING FREQUENCIES ON THE RESULTS OF MUTUAL INDUCTANCE IDENTIFICATION

Different ranges of ω	Different solution situations of $M_{2,3}$
$\omega < \omega_{Lp} < \omega_{os}$	$X_s < 0,\ X_{Lp} < 0, X_{Lp}X_s - R_{Lp}R_s > 0,$ $M_{2,3}$ have real solutions
$\omega_{Lp} \le \omega \le \omega_{os}$	$X_s \le 0,\ X_{Lp} \ge 0, X_{Lp}X_s - R_{Lp}R_s \le 0,$ $M_{2,3}$ have no real solutions
$\omega_{Lp} < \omega_{os} < \omega$	$X_s > 0, X_{Lp} > 0, X_{Lp}X_s - R_{Lp}R_s > 0,$ $M_{2,3}$ have real solutions

1) When the working angular frequency satisfies $\omega_{Lp} = \sqrt{\frac{1}{L_pC_p}} \le \omega \le \omega_{os}$, $X_s \le 0$ and $X_{Lp} \ge 0$ will be satisfied automatically. In this case, $X_{Lp}X_s - R_{Lp}R_s \le 0$ will be satisfied, which means $M_{2,3}$ have no real solutions.
2) When the working angular frequency satisfies $\omega < \omega_{Lp} < \omega_{os}$, $X_s < 0$ and $X_{Lp} < 0$ will be satisfied automatically. In this case, $X_{Lp}X_s - R_{Lp}R_s > 0$ will be satisfied, that is, $M_{2,3}$ have real solutions.
3) When the working angular frequency satisfies $\omega_{Lp} < \omega_{os} < \omega$, $X_s > 0$ and $X_{Lp} > 0$ will be satisfied automatically. In this case, $X_{Lp}X_s - R_{Lp}R_s > 0$will be satisfied, $M_{2,3}$ have real solutions, too.

The existence of real solutions for $M_{2,3}$ shows that the function $y = f(M)$ has extremal points at the real solutions, which means that $y = f(M)$ does not have unique monotonicity. The $|Z_p|$ calculated by measured value is not a one-to-one relationship with M. In this case, it is possible to find multiple solutions that meet the conditions according to (9), which will affect the identification results.

According to the above analysis, the influence of the operating frequency on the solution of $M_{2,3}$ is summarized in Table I.

In order to avoid the situation where there are multiple real solutions in M_{iden}, the frequency range $\omega_{Lp} \le \omega \le \omega_{os}$ used in the mutual inductance identification is recommended. When $\omega_{Lp} \le \omega \le \omega_{os}$ is satisfied, there is only an extremal point at $M = 0$ in (9), and $|Z_p|$ and M have a one-to-one relationship when $M > 0$. Hence, the unique solution of M can be identified based on the measured value of U_{c1_mea} and I_{p_mea}

Combined with (9), when the frequency of $\omega_{Lp} \le \omega_{\text{iden}} \le \omega_{os}$ is adopted for mutual inductance identification, (12) shown at the bottom of this page, can be obtained from (9). Substituting the measured values U_{c1_mea} and I_{p_mea} into (12), and then the unique solution of mutual inductance identification value M_{iden} can be obtained by solving (12) shown at bottom of next page. In (12), $\omega_{\text{iden}} = 2\pi f_{\text{iden}}$, f_{iden} is the frequency in the mutual inductance identification phase, and satisfies $\frac{1}{2\pi}\omega_{Lp} \le f_{\text{iden}} \le \frac{\omega_{os}}{2\pi}$. When the parameter design is done according to (5), the inequality $\omega_{Lp} \le \omega_{os}$ will be satisfied automatically. Therefore, the requirement of $\frac{1}{2\pi}\omega_{Lp} \le f_{\text{iden}} \le \frac{\omega_{os}}{2\pi}$ in the mutual inductance identification phase does not add additional constraints to the parameter design of the system.

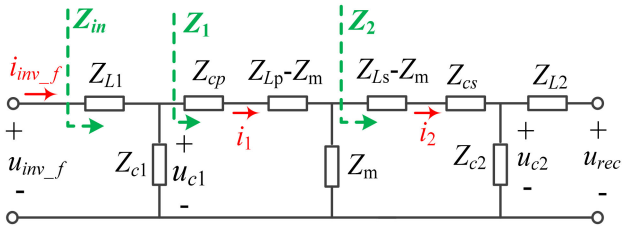

Fig. 5. Equivalent circuit diagram when load is decoupled.

B. Analysis of U_{dc} and Conduction Angle α for Load Decoupling

From the analysis in Section II-B, it can be found that when (4) is satisfied, the rectifier bridge on the secondary side is always open and the load is decoupled from the system. According to the fundamental wave approximation method, the equivalent circuit of the system is shown in Fig. 5, and (13) can be further derived from (4)

$$U_{\text{rec}f_{p\text{iden}}}\left(U_{\text{inv}f_{p\text{iden}}}\right) = U_{c2_p} < U_{\text{Bat}_{\min}}. \tag{13}$$

That is, the open circuit voltage in front of the rectifier is equal to the voltage on the compensation capacitor C_2, and its amplitude is less than $U_{\text{Bat\_min}}$.

Each impedance in Fig. 5 satisfies the following equation:

$$\begin{cases} Z_2 = Z_{Ls} - Z_m + Z_{cs} + Z_{c2} \\ Z_1 = Z_{cp} + Z_{Lp} - Z_m + Z_2 \ \ //Z_m \\ Z_{\text{in}} = Z_{L1} + Z_{c1}//Z_1 \end{cases} \tag{14}$$

where $Z_{L1} = R_1 + j\omega L_1$, $Z_{cp} = 1/j\omega C_p$, $Z_{c1} = 1/j\omega C_1$, $Z_{Lp} = R_{Lp} + j\omega L_p, Z_m = j\omega M, Z_{Ls} = R_{Ls} + j\omega L_s, Z_{cs} = 1/j\omega C_s$, and $Z_{c2} = 1/j\omega C_2$.

Therefore, when the (13) is satisfied, the fundamental component amplitude of the inverter output voltage $U_{\text{inv\_}f\_p\_\text{iden}}$ and the voltage amplitude U_{c2_p} on the capacitor C_2 satisfies (15), where $|Z_{\text{eq}}(M)|$ is the absolute value of the equivalent impedance including the mutual inductance M

$$\begin{aligned} U_{c2\_p} &= \left|\frac{Z_{c1}Z_mZ_{c2}}{Z_{\text{in}}\left(Z_1 + Z_{c1}\right)\left(Z_2 + Z_m\right)}\right| U_{\text{inv}\_f\_\text{iden}} \\ &= \left|Z_{\text{eq}}\left(M\right)\right| U_{\text{inv}\_f\_\text{iden}}. \end{aligned} \tag{15}$$

Combining (1), (2), (13), and (15), the conditions required to achieve load decoupling in the two soft start modes are obtained, respectively, as (16) and (17) shows

$$\alpha_{\text{iden}} < \arcsin\frac{\pi U_{\text{Bat\_min}}}{4U_{\text{dc\_set}}\left|Z_{\text{eq}}\left(M\right)\right|} \tag{16}$$

$$U_{\text{dc\_iden}} < \frac{\pi U_{\text{Bat\_min}}}{4\left|Z_{\text{eq}}\left(M\right)\right|\sin\left(\frac{\pi-\theta}{2}\right)} \tag{17}$$

$$M_{\text{iden}} = \frac{1}{\omega_{\text{iden}}}\sqrt{X_{Lp}X_s - R_sR_{Lp} + \sqrt{\left(R_sR_{Lp} - X_{Lp}X_s\right)^2 - \left(R_s^2 + X_s^2\right)\left(R_{Lp}^2 + X_{Lp}^2 - \left|\frac{U_{c1_{\text{mea}}}}{I_{p_{\text{mea}}}}\right|^2\right)}} \tag{12}$$

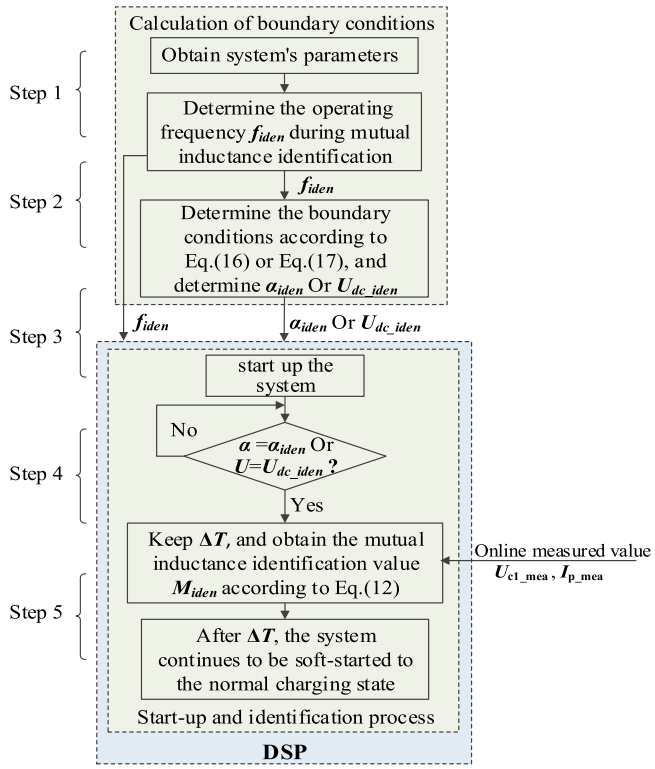

Fig. 6. Flowchart of the proposed mutual inductance identification method.

where $\alpha_{\rm iden}$ and $U_{\rm dc\_iden}$ are the conduction angle and the dc input voltage for load decoupling, respectively.

In (16) and (17), $U_{\rm Bat\_min}$ is the battery discharge cut-off voltage, θ is the inverter dead time, and $U_{\rm dc\_set}$ is the rated dc input voltage. The above parameters are known in the system design stage. Therefore, after the system is designed, the boundary conditions of $\alpha_{\rm iden}$ and $U_{\rm dc\_iden}$ for load decoupling can be determined by the (16) and (17) and the change trend of $|Z_{\rm eq}(M)|$ with the change of mutual inductance. The realization process of load decoupling will be elaborated in detail based on the actual system parameters in Section V-B.

C. Realization Process of the Proposed Mutual Inductance Identification Method

According to the aforementioned analysis, detailed mutual inductance identification process of the proposed method, shown in Fig. 6, is described as follows.

Step 1: The system parameters are obtained, and the operating frequency $f_{\rm iden}$ during mutual inductance identification period is determined according to the system parameters.

Step 2: The boundary conditions of load decoupling are determined, and $\alpha_{\rm iden}$ or $U_{\rm dc\_iden}$ during the mutual inductance identification is determined. When the variable conduction angle method is used to realize soft start, the $\alpha_{\rm iden}$ is determined according to the system parameters and (16). When the variable input dc voltage method is used to realize soft start, the $U_{\rm dc\_iden}$ is determined according to the system parameters and (17).

Step 3: According to the determined value of $f_{\rm iden}$, and $\alpha_{\rm iden}$ or $U_{\rm dc\_iden}$, the soft start control program is written in the microcontroller combined with the mutual inductance identification algorithm.

Step 4: Start the system, when $\alpha=\alpha_{\rm iden}$ or $U_{\rm dc}=U_{\rm dc\_iden}$, keep this state for ΔT. Substituting the measured values $U_{\rm c1\_mea}$ and $I_{p\_\rm mea}$ into (12) to obtain the mutual inductance identification value $M_{\rm iden}$ during ΔT. The ΔT is determined by the time required for the system from transient to steady state including detection, DSP calculation and a certain amount of time margin.

Step 5: After ΔT, the system continues to soft start-up until it reaches the normal charging state.

IV. Research on Parameter Sensitivity

A. Theoretical Analysis of Parameter Sensitivity

In practical, due to the magnetic material in the coupler module, the self-inductance of coil will change with the longitudinal distance and lateral dislocation between the two coils [37], [38]. Therefore, it is necessary to analyze and discuss the sensitivity of the identification algorithm to the self-inductance parameters of the coil. The existing literature on mutual inductance identification rarely discusses the influence of the change of coil self-inductance on the accuracy of the identification algorithm in detail.

Equation (9) directly reflects the relationship between *M* and $|Z_p|$, so it is used to analyze the sensitivity of the algorithm to the slight changes in L_p and L_s. To simplify the analysis process, define A and B as follows:

$$\begin{cases} A=\frac{(\omega M)^2 R_s}{R_s^2+X_s^2}+R_{Lp}=CR_s+R_{Lp}\approx CR_s \\ B=X_{Lp}-\frac{(\omega M)^2 X_s}{R_s^2+X_s^2}=X_{Lp}-CX_s=X_{Lp}+C\,|X_s| \end{cases} \tag{18}$$

where $C=\frac{(\omega M)^2}{R_s^2+X_s^2}$.

Equation (19) can be obtained according to (9) and (18)

$$|Z_p|=\sqrt{A^2+B^2}. \tag{19}$$

According to the authors in [39], parameter sensitivity is analyzed though the derivative. Since the changes of L_p and L_s are reflected in the impedances X_{Lp} and X_{Ls}, the derivation calculation results of $\partial|Z_p|/\partial X_{Lp}$ and $\partial|Z_p|/\partial X_{Ls}$ are given by (20) and (21), respectively

$$\frac{\partial\,|Z_p|}{\partial X_{Lp}}=\frac{B}{\sqrt{A^2+B^2}} \tag{20}$$

$$\frac{\partial\,|Z_p|}{\partial X_{Ls}}=(\omega M)^2\frac{2AR_sX_s+B\left(X_s^2-R_s^2\right)}{\left(X_s^2-R_s^2\right)^2\sqrt{A^2+B^2}}. \tag{21}$$

Comparing *A* and *B* according to (18), it can be found that *A* will be very small and much smaller than *B* due to $R_s\approx 0$, that is, $A^2\ll B^2$. Therefore, (20) can be simplified to (22), that is, 1% deviation of X_{Lp} contributes to about 1% deviation of $|Z_p|$

$$\frac{\partial\,|Z_p|}{\partial X_{Lp}}=\frac{B}{\sqrt{A^2+B^2}}\approx 1. \tag{22}$$

TABLE II
COUPLING COIL PARAMETERS

Parameter	Value	Parameter	Value
Coil turns	14	Coil outer circle size (mm)	450*450
Number of coil wire strands	1000	Coil inner circle size (mm)	200*200
The radius of strands (mm)	0.05		

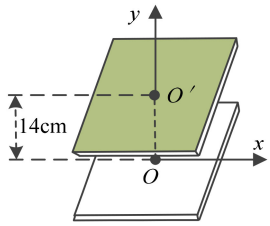

Fig. 7. Two definitions of misalignments: *x*-misalignment is the lateral misalignment, and *y*-misalignment is the longitudinal distance.

Equation (21) shows that the derivative is affected by X_{Ls}. So, the relationship between $|Z_p|$ and M is sensitive with X_{Ls}. In addition, the derivative is also affected by ω and M, which means that $|Z_p|$ has different sensitivity to X_{Ls} under different ω and M conditions.

B. Simulation Verification of Parameter Sensitivity

The parameters of the coupling coils used in this system are shown in Table II. The dimensions and parameters of the two square coils are the same. The relative position of the two coils is shown in Fig. 7, and the position shown in Fig. 7 is the alignment of the two coils. The longitudinal distance between the two coils is along the *y* direction, and the translation along the *x* direction is a lateral displacement. In the rest of this article, the coil position will be represented by (*x*, *y*) and will not be repeated.

Change the *y* and *x* between the two coils, and then the coil parameters L_p, L_s, and M at different positions (*x*, *y*) will be obtained through measurement. The measured results are shown in Fig. 8. It can be seen that the parameter L_p and L_s decrease with the increase of *y*. When $y > 14$ cm, the decreasing trend of L_p and L_s slows down. When *y* is constant and 0 cm $< x <$ 12 cm, L_p and L_s will increase slowly with the increase of *x*.

The designed coupling coefficient of the system is $0.1 \leq k \leq 0.2$, the allowable position range is 14 cm $< y <$ 16 cm, and 0 cm $< x <$ 12 cm. The variation of the parameters L_p, L_s, and M within this range are shown in Fig. 9. It can be seen that under the same *y*, the coil self-inductance increases slowly with the increase of *x*. When the *x* reaches 12 cm, the self-inductance variation is close to 1 μH. Therefore, simply substituting a certain self-inductance value as a known parameter into the algorithm will affect the identification result. The sensitivity of the algorithm to the microvariation of the self-inductance should be analyzed, then the self-inductance value should be corrected to improve the identification accuracy.

Based on the actual parameters of the system in Table III and the measured parameters in Figs. 8 and 9, the sensitivity of the system to the L_p and L_s is further studied, and the results are shown in Figs. 10 and 11.

Fig. 10 shows the results of studying the sensitivity of Z_p to L_p at different frequencies. It can be seen from the Fig. 10 that when the change of L_p reaches 1 μH, the variation of Z_p is also very small. When ΔL_p is fixed, ΔZ_p is slightly different with the frequency. These results proved the correctness of the aforementioned conclusion, that is, the algorithm is not sensitive to L_p and has good robustness to L_p.

Since the L_s at positions (*x*, *y*) = (12, 14) and (*x*, *y*) = (0, 16) have the largest change relative to L_s at the alignment position, these two positions are taken as examples to study the influence of ΔL_s on Z_p. The results are shown in Fig. 11. It can be seen that when the frequency and ΔL_s are constant, ΔZ_p is related to M, the smaller M is, the smaller ΔZ_p will be. When the mutual inductance M and ΔL_s are constant, ΔZ_p is related to f_{iden}, and the smaller f_{iden} is, the smaller ΔZ_p will be. The above results prove the correctness of the aforementioned conclusion, that is, the algorithm is sensitive to L_s, and its sensitivity is related to ω and M. Therefore, according to the above analysis results, a smaller identification frequency f_{iden} should be selected to reduce the identification error.

V. SIMULATION, EXPERIMENTAL VERIFICATION, AND DISCUSSION

A. Experimental Platform and System Parameters

A WPT prototype shown in Fig. 12 is developed to verify the presented mutual inductance identification method, and its parameters are shown in Table III. Parameters are measured by *LCR* Meter TH2826 at 85 kHz. The normal charging frequency of the system is 84–85 kHz. Among them, the parameters L_p and L_s are measured when (*x*, *y*) = (0, 14).

B. Calculation and Simulation Verification of Load Decoupling Boundary Conditions

According to Section III-A, during load decoupling stage, when the frequency of $\text{sqrt}(1/L_p/C_p)/2/\pi \leq f_{\text{iden}} \leq \omega_{os}/2/\pi$ is used for M identification, the unique solution of M identification value M_{iden} can be obtained by solving (12). According to the system parameters in Table III, $\text{sqrt}(1/L_p/C_p)/2/\pi = 78693$(Hz), $\omega_{os}/2/\pi = 84636$(Hz). In order to verify whether the conclusions in Table I are correct or not, simulations are performed when $f_{\text{iden}} < \text{sqrt}(1/L_p/C_p)/2/\pi$(75–78 kHz), $\text{sqrt}(1/L_p/C_p)/2/\pi \leq f_{\text{iden}} \leq \omega_{os}/2/\pi$(80–83kHz), and $f_{\text{iden}} > \text{sqrt}(1/L_p/C_p)/2/\pi$(85–88 kHz), and the $|Z_p| - M$ relationship curve at different frequencies are obtained as shown in Fig. 13.

It can be seen that when $sqrt(1/L_p/C_p)/2/\pi \leq f_{\text{iden}} \leq \omega_{os}/2/\pi$(80 kHz, 81 kHz, 82 kHz, 83 kHz), $|Z_p|$ increases monotonously with M, and there is no extremal point in the range of $M > 0$. In other words, $|Z_p|$ and M have a one-to-one correspondence. When $f_{\text{iden}} < \text{sqrt}(1/L_p/C_p)/2/\pi$(75 kHz, 76 kHz, 77 kHz, 78 kHz) or $f_{\text{iden}} > \text{sqrt}(1/L_p/C_p)/2/\pi$(85 kHz, 86 kHz, 87 kHz, 88 kHz),

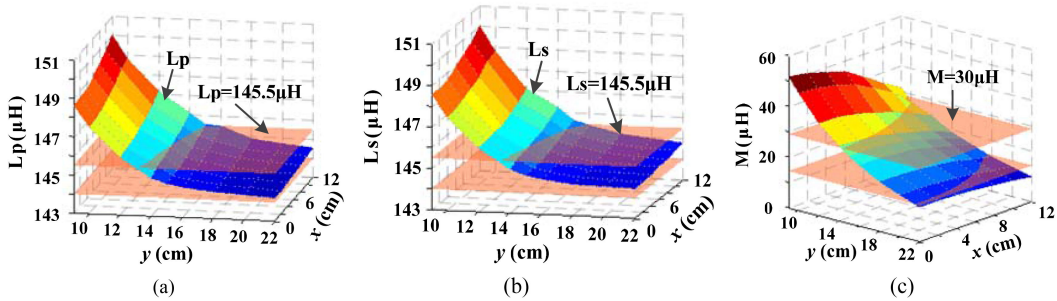

Fig. 8. Change trend chart of L_p, L_s, and M under different position (x, y). (a) Change trend chart of Lp. (b) Change trend chart of Ls. (c) Change trend chart of M.

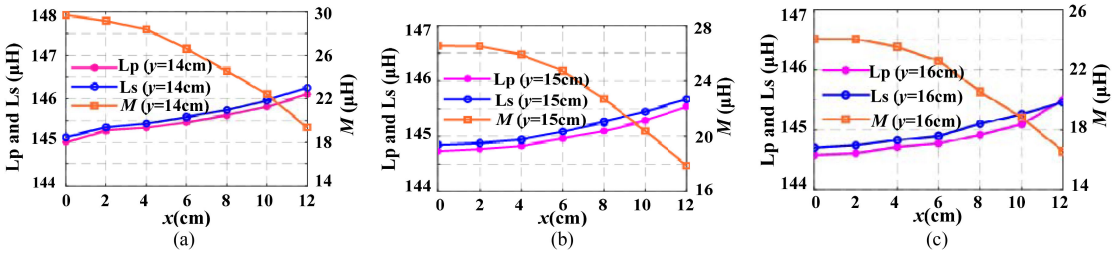

Fig. 9. Variation of L_p, L_s, and M with x under different y. (a) When $y = 14$ cm. (b) When $y = 15$ cm. (c) When $y = 16$ cm.

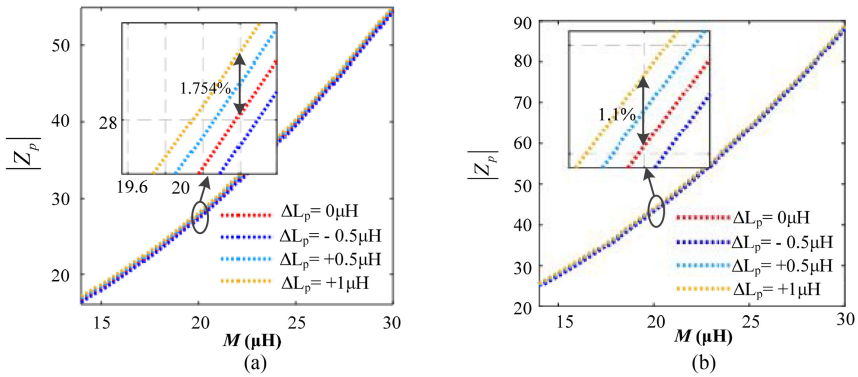

Fig. 10. Results of the sensitivity of $|Z_p|$ to L_p at different frequencies. (a) Influence of ΔL_p on $|Z_p|$ when $f = 80$kHz. (b) Influence of ΔL_p on $|Z_p|$ when $f = 83$kHz.

TABLE III
SYSTEM'S PARAMETERS

Parameter	Value
$L_p(\mu\text{H})/R_{Lp}(\text{m}\Omega)$	145/360
$L_s(\mu\text{H})/R_{Ls}(\text{m}\Omega)$	145.12/350
$L_1(\mu\text{H})/R_{L1}(\text{m}\Omega)$	25.2/30
$L_2(\mu\text{H})/R_{L2}(\text{m}\Omega)$	51.2/570
$C_1(\text{nF}), C_P(\text{nF})$	138.25, 28.21
$C_2(\text{nF}), C_s(\text{nF})$	68.57, 37.8
k	0.1-0.2
$U_{Bat\_min}(\text{V})$	300
$U_{dc\_set}(\text{V})$	250

$|Z_p| = f(M)$ has an extremal point and does not have unique monotonicity. The correctness of the conclusions in Section III-A and Table I is proved by simulation results mentioned above.

According to the system parameters, $U_{\text{Bat\_min}}$ and (15)–(17), the relationship between U_{c2_p}, f_{iden}, $U_{\text{inv\_f\_p}}$, and M is obtained through simulation, shown in Fig. 14. In Fig. 14, the change trend of U_{c2_p} with M and $U_{\text{inv\_f\_p}}$ when f_{iden} equals to 80, 81, 82, and 83 kHz are illustrated from (a) to (d), respectively.

The maximum coupling coefficient of the system is $k_{\max} = 0.2$ ($M_{\max}$ is about 30 μH). It can be seen from Fig. 14 that if k ranges from 0.1 to 0.2 and $U_{\text{inv\_f\_p}}$ maintain a constant value, U_{c2_p} will change monotonically with M when f_{iden} increases from 80 to 83 kHz. Therefore, to ensure the load decoupling in the whole range of coupling coefficient, U_{c2_p} is only required to be lower than $U_{\text{Bat\_min}}$ at $M = 30\mu$H.

Meanwhile, it can be seen from Fig. 14 that at $M = 30\mu$H, when $U_{c2_p} = U_{\text{Bat_min}} = 300$V, the corresponding $U_{\text{inv\_f\_p}}$ are 96, 77, 57, and 37 V, respectively. Solving (1) and (2), the boundary conditions for the system to achieve load decoupling

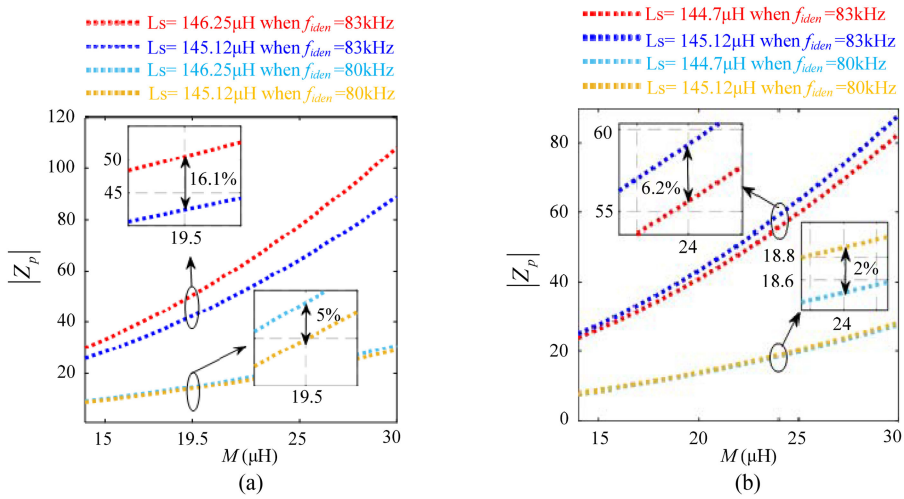

Fig. 11. Effect of the change of L_s at a special position relative to the aligned position on $|Z_p|$ at different frequencies. (a) Influence of the change of L_s at $(x, y) = (12, 14)$ relative to L_s at the alignment position on $|Z_p|$. (b) Influence of the change of L_s at $(x, y) = (0, 16)$ relative to L_s at the alignment position on $|Z_p|$.

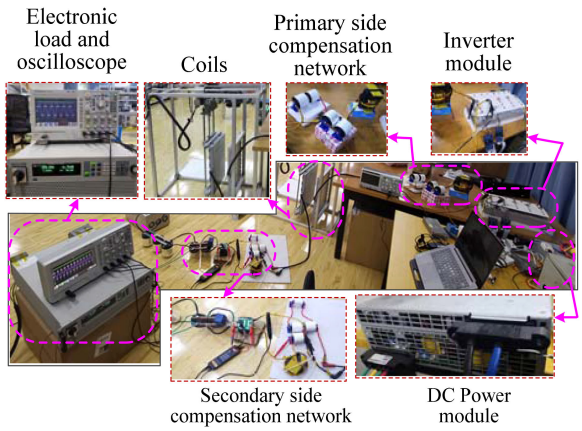

Fig. 12. Schematic diagram of the experimental platform.

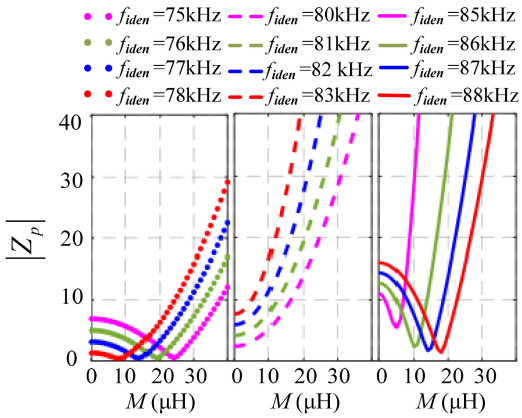

Fig. 13. Relationship between $|Z_p|$ and M at different frequencies.

are shown in Table IV. That is, when the system runs under the conditions of Table IV, the load is decoupled, and the identification method proposed in this article can be used to identify the mutual inductance.

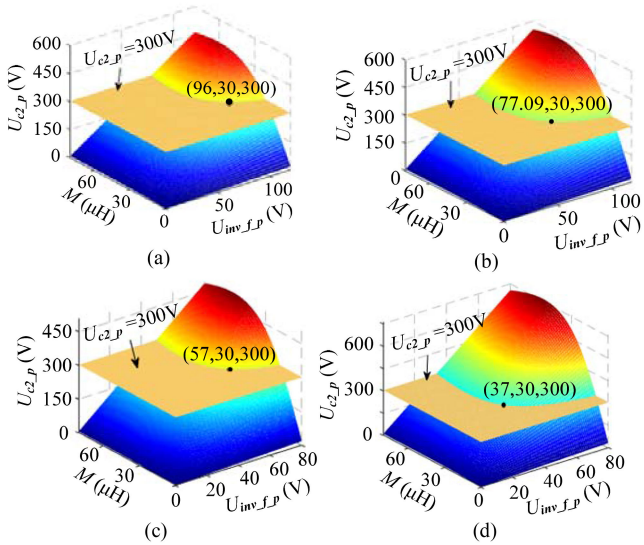

Fig. 14. Variation trend of U_{c2_p} with M and $U_{\mathrm{inv}\_f\_p}$ under different f_{iden}, (a) when $f_{\mathrm{iden}} = 80$kHz, (b) when $f_{\mathrm{iden}} = 81$kHz, (c) when $f_{\mathrm{iden}} = 82$kHz, and (d) when $f_{\mathrm{iden}} = 83$kHz.

TABLE IV
SUMMARY OF WORKING POINT AREAS THAT CAN REALIZE M IDENTIFICATION

Conditions for load decoupling	Soft start methods	
	Soft start method (a), $U_{dc_set} = 250$V	Soft start method (b), $\alpha = \pi$
$f_{iden} = 80$kHz, $U_{inv_f_p} < 96$V	$\alpha < 35°$	$U_{dc} < 75$V
$f_{iden} = 81$kHz, $U_{inv_f_p} < 77$V	$\alpha < 28°$	$U_{dc} < 60.6$V
$f_{iden} = 82$kHz, $U_{inv_f_p} < 57$V	$\alpha < 20.7°$	$U_{dc} < 45$V
$f_{iden} = 83$kHz, $U_{inv_f_p} < 37$V	$\alpha < 13°$	$U_{dc} < 29$V

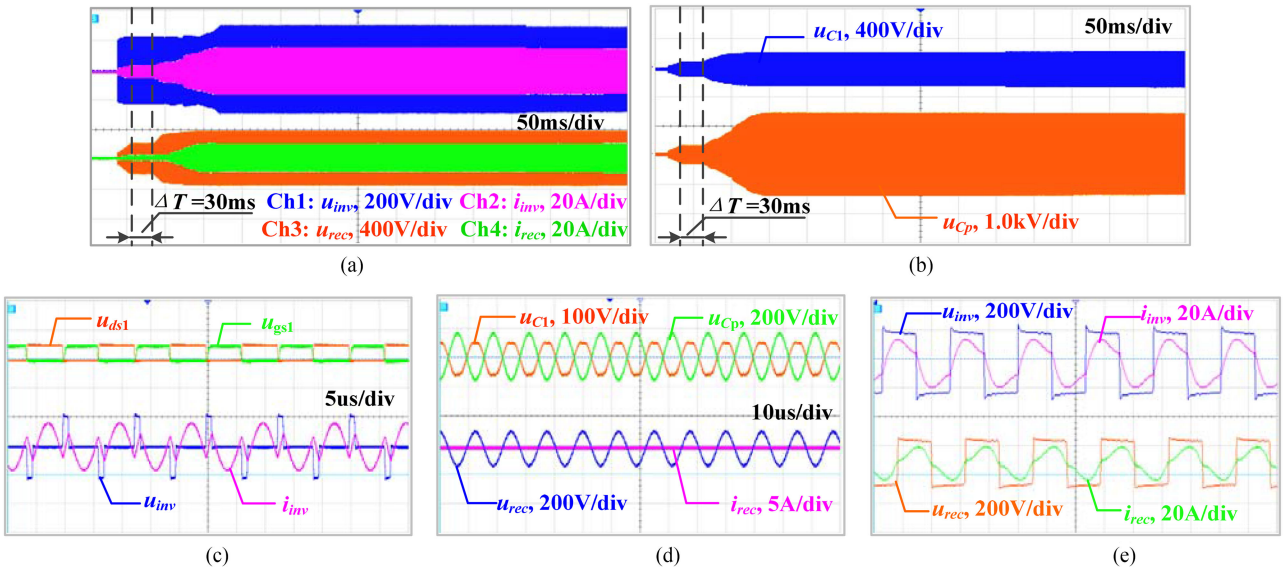

Fig. 15. Waveforms obtained when the soft start method (a) is adopted, and $f_{\mathrm{iden}} = 80\mathrm{kHz}$, $\alpha = 30°$ is used to achieve load decoupling. (a) and (b) are dynamic experimental results during soft start, (c) and (d) are waveforms at the identification stage, and (e) is the waveforms during normal operation.

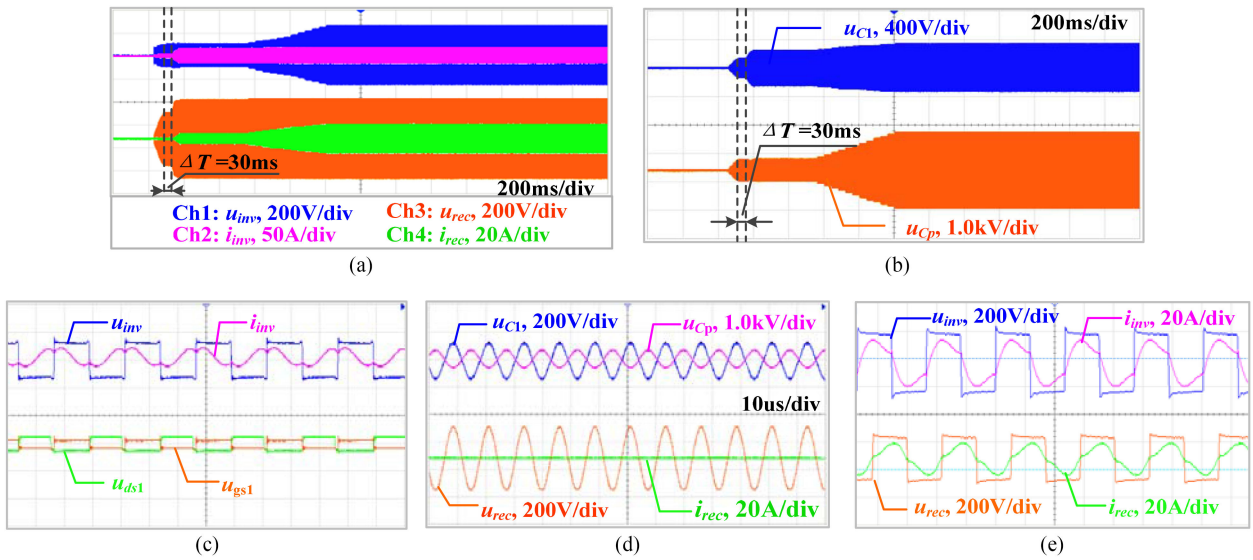

Fig. 16. Waveforms obtained when the soft start method (a) is adopted, and $f_{\mathrm{iden}} = 80\mathrm{kHz}$, $U_{\mathrm{dc}} = 60\mathrm{V}$ is used to achieve load decoupling. (a) and (b) are dynamic experimental results during soft start, (c) and (d) are waveforms at the identification stage, and (e) is the waveforms during normal operation.

C. Experimental Verification and Discussion

In order to prove the feasibility of load decoupling during soft-start process and the correctness of mutual inductance identification method proposed, experimental verification is carried out by using the experimental platform shown in Fig. 12. The input dc voltage is provided by the dc power supply (REG75030), and the output voltage of which is controlled by the host computer. Set the electronic load to work in constant voltage (CV) mode with 300 V to simulate the initial voltage of the battery. The soft start control process and mutual inductance identification algorithm are implemented based on DSP (TMS320F28335).

First, experiment is implemented to verify whether the load decoupling can be realized during the soft-start process. Two open-loop soft-start methods described in Section II-B were tested, and the experimental results are shown in Figs. 15 and 16.

Fig. 15 shows the experimental results when the soft start method (a) is adopted. The soft-start control process is as follows: First of all, in the case of $f = 80\mathrm{kHz}$ and $U_{\mathrm{dc}} = 200\mathrm{V}$, the conduction angle α is controlled to increase from 0°to 30°. Second, when $\alpha = 30°$, keep this state for $\Delta T = 30$ ms, and the load is decoupled and mutual inductance identification can be performed at the time. Then, α is controlled to continue

to increase to 178° (with a dead time of 2°). Finally, the host computer sends a command to the DSP to control the frequency of the drive signal to ramp up from 80 to 85 kHz. Fig. 15(a) and (b) are dynamic experimental results, Fig. 15(c) and (d) are waveforms at the identification stage, and Fig. 15(e) is the waveforms during normal operation. It can be seen from Fig. 15(a) and (b) that there will be no high current and voltage overshoot. Fig. 15(c) and (d) are the experimental results during ΔT. It can be seen that the MOSFET is working in the ZVS state at this time, and the load is decoupled ($i_{\rm rec} = 0$A and $u_{\rm rec} < 300$V). After the soft start process is over, the system is in the normal charging mode, as shown in Fig. 15(e).

Fig. 16 shows the experimental results when the soft start method (b) is adopted. The soft-start control process is as follows. First, in the case of $f = 80$kHz , $U_{\rm dc}$ is controlled by host computer to increase from 0 to 60 V. Second, when $U_{\rm dc} = 60$V, keep this state for $\Delta T = 30$ ms, and the load is decoupled and mutual inductance identification can be performed at the time. Then, the frequency of drive signal is controlled to ramped up from 80 to 85 kHz. Finally, the $U_{\rm dc}$ is controlled by host computer to increase from 60 to 200 V. Similarly, there will be no high current and voltage overshoot during the starting process, and the load is decoupled during ΔT. It should be noted that during the load decoupling phase, the MOSFET may lose ZVS. Fig. 16(c) is the waveforms of the load decoupling stage when $M = 29.8$ μH. It can be seen that the MOSFET loses ZVS at this time. However, the time of soft-start process and identification process is very short, and the mutual inductance identification is implemented under the condition of small voltage and current, so the missing of ZVS transitorily will not bring large energy loss and switching stress.

Second, during ΔT in Fig. 16, the correctness of the mutual inductance identification method was experimentally verified based on the measured U_{c1} and U_{cp}. Two voltage effective value detection modules are used to detect U_{c1} and U_{cp}. The output dc voltage signal of the detection module (reflecting the rms of the measured voltage) is sent to the DSP after signal conditioning circuit, and the calculation process of identification algorithm is completed in DSP. In order to reduce the influence of harmonic components and noise on the measurement accuracy, the adopted detection modules composed of prefilter circuit, high-precision rectifier filter circuit and high-linearity analog optocouplers are used to improve the measurement accuracy. In order to reduce the detection error, I_p is obtained by detecting the U_{cp} since I_p is too small and might cause inaccurate detection. Then, the U_{cp} to I_p are converted in DSP according to $I_p = 2\pi f_{\rm iden} \cdot C_p \cdot U_{cp}$.

To verify the feasibility of the identification algorithm and the correctness of the parameter sensitivity analysis, the mutual inductance values at different positions are obtained by changing the lateral misalignment x under the three cases of $y = 14$ cm, 15 cm, and 16 cm. The mutual inductance M at different positions is identified by using the method proposed in this article, and the identification results and errors are shown in Fig. 17. In Fig. 17, the ordinate value on the left represents the M measured at different (x, y), and the ordinate on the right represents the identification error, the blue bar represents the error, and the

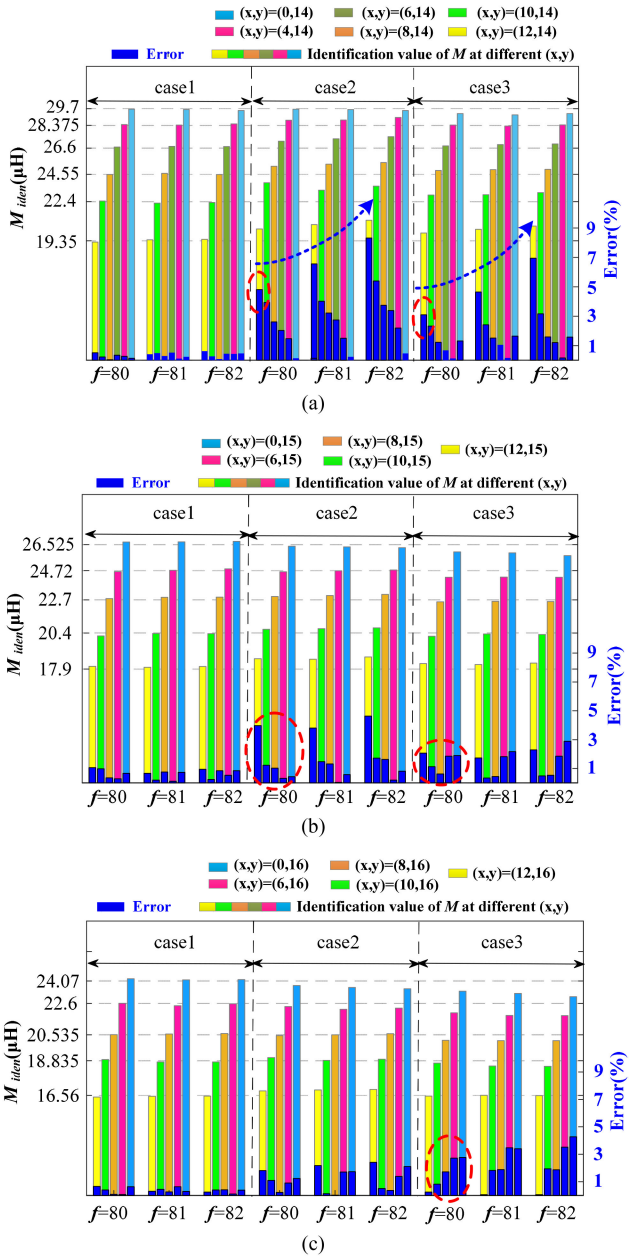

Fig. 17. Experimental results and errors of $M_{\rm iden}$ under different conditions. (a) Experimental results and errors of $M_{\rm iden}$ when $y = 14$ cm. (b) Experimental results and errors of $M_{\rm iden}$ when $y = 15$ cm. (c) Experimental results and errors of $M_{\rm iden}$ when $y = 16$ cm.

other bars represent the identification results of M at different (x, y). In particular, three cases are designed to prove the correctness of the aforementioned parameter sensitivity analysis. Case 1 substitutes the actual self-inductance measured at each position into the algorithm to obtain the identification result. Case 2 substitutes the self-inductance at alignment position (x, y) = (0, 14) into the algorithm to obtain the identification result. Case 3 substitutes the $L_{p\_\rm ave}$ and $L_{s\_\rm ave}$ into the algorithm to obtain the identification result. According to the self-inductance value of the coil measured in Fig. 9, the average value of the coil self-inductance is $L_{p_\rm ave} = 145.34\mu$H and $L_{s_\rm ave} = 145.475\mu$H. In

Fig. 17, $f_{\text{iden}} = 80$ kHz, 81 kHz, and 82 kHz are used for mutual inductance identification in the identification algorithm.

The following conclusions can be obtained by analyzing the experimental results from Fig. 17.

1) In case 1, the proposed identification method can identify the M accurately, and the max identification error ($\text{error}_{\max}$) is less than 1%, which means that the mutual inductance M can be well recognized by the proposed algorithm when the self-inductance parameters are known, and the recognition accuracy is very high.

2) In practice, it is unrealistic to measure the self-inductance value of the coil before each system operation. Generally, the self-inductance in the case of coil alignment is substituted into the algorithm. Therefore, the self-inductance $L_p = 145\mu$H, $L_s = 145.12\mu$H corresponding to the coil alignment position (that is, the position $(x, y) = (0, 14)$) is substituted into the algorithm for experiment, and the experimental results correspond to case 2 in Fig. 17. By comparing the identification results of cases 1 and 2, it is not difficult to find that the existence of ΔL_p and ΔL_s increases the identification error. In case 2, when $f_{\text{iden}} = 82$kHz is used for mutual inductance identification, the $\text{error}_{\max}$ is higher than 8%, and when $f_{\text{iden}} = 80$Hz is used for mutual inductance identification, the $\text{error}_{\max}$ is less than 5%. Hence, the smaller f_{iden} is used, the smaller identification error will be, which also verifies the correctness of the previous conclusions of the parameter sensitivity analysis. Therefore, using a smaller f_{iden} for mutual inductance identification can effectively improve the identification accuracy.

3) In order to further reduce the identification error at the maximum misalignment case, the average value of the self-inductance is calculated within the allowable misalignment range. $L_{p_\text{ave}} = 145.34\mu$H and $L_{s_\text{ave}} = 145.475\mu$H are obtained according to the measurement results in Fig. 9. L_{p_ave}, L_{s_ave} are substituted into the identification algorithm, and the identification results correspond to case 3 in Fig. 17. By comparing the identification results of cases 2 and 3 under the same identification frequency, it can be found that the maximum error in case 3 is significantly smaller than the maximum error in case 2, which shows the maximum identification error can be effectively reduced by means of self-inductance correction. In case 3, the identification error when f_{iden} is 80 kHz is significantly smaller than the error when f_{iden} is 82 kHz, which also proves that a smaller f_{iden} can reduce the identification error effectively. From the results in case 3, it can be found that the $\text{error}_{\max}$ will be less than 4% when the self-inductance is corrected and a smaller f_{iden} is selected for mutual inductance identification.

Fig. 18 shows the identification results when $f_{\text{iden}} = 80$kHz in case 3. It can be found that the identification $\text{error}_{\max}$ is only 3.1% when the lateral dislocation is allowed to be 12 cm, and the error is within the acceptable range. Compared with the existing partial mutual inductance identification methods, the mutual inductance identification method proposed in this article has much better performance without compromising the identification accuracy (in [15], the identification $\text{error}_{\max}$ is 8% when the lateral dislocation is 10 cm. In [16], the identification $\text{error}_{\max}$ is 6.5%. In [17], the identification $\text{error}_{\max}$ when changing the load and changing the mutual inductance are 7% and 2.9%, respectively. In [21], the identification $\text{error}_{\max}$ is 4.87% when the longitudinal distance changes). Detailed comparison can be found in Table V shown below.

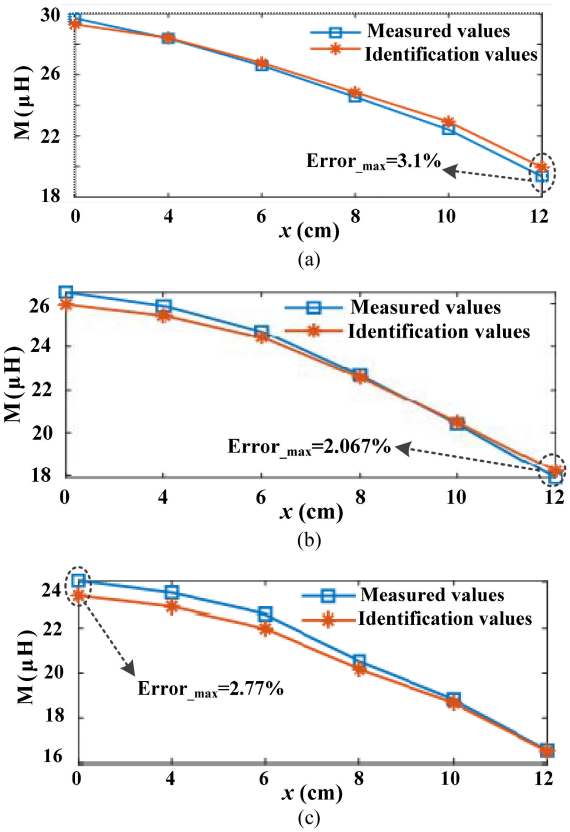

Fig. 18. Identification results of M_{iden} when $f_{\text{iden}} = 80$kHz in case3. (a) Experimental results when $y = 14$ cm. (b) Experimental results when $y = 15$cm. (c) Experimental results when $y = 16$ cm.

TABLE V
COMPARISON OF THE FEATURES OF DIFFERENT METHODS ON MUTUAL INDUCTANCE IDENTIFICATION

Features	[15]	[16]	[17]	[21]	Proposed
No need to measure the phase difference between voltage and current	√	×	×	×	√
No need to add auxiliary circuit	√	√	×	√	√
No need to use switches to achieve load decoupling	√	√	√	×	√
No need to calculate phase difference for identification	×	√	√	√	√
The identification error_{max}	8%	6.5%	7%	4.8%	3.1%

D. Further Discussion

To sum up, using the load decoupling method and mutual inductance identification method proposed in this article, mutual inductance identification can be effectively carried out at the initial stage of system soft-start with high identification accuracy, which does not affect the system's normal operation. Moreover, there is no need to measure the phase difference between voltage

and current, auxiliary circuits and switches are also saved to achieve load decoupling. In addition, the proposed method is suitable for other nonseries compensation topologies on the secondary side, and has strong universality.

It should be noted that the proposed method is based on the condition that the compensation network parameters are known and unchanged. For a stable IPT system, except for the load and mutual inductance, all circuit parameters change little under normal operating conditions. Therefore, the method proposed in this article is applicable within the allowable deviation range. When the self-inductance parameter has a large deviation due to large misalignment, the identification error may increase. Therefore, in order to improve the identification accuracy when the parameter deviation is large, further work will be focused on investigating the identification methods that do not require known coil parameters.

VI. Conclusion

A general load decoupling method is proposed, which can be used to realize mutual inductance identification for multiple topologies. Taking the double-sided *LCC* topology as an example, a mutual inductance identification method is presented under the proposed load decoupling method. The mutual inductance identification method presented in this article needs neither secondary side switches to achieve load decoupling nor auxiliary circuits to switch the circuit working mode. It requires only soft-start process and battery initial voltage to realize load decoupling, which reduces system complexity and saves system costs. Through the detailed theoretical analysis and derivation of the presented method, the main conclusions are given as follows.

1) When $\mathrm{sqrt}(1/L_p/C_p)/2/\pi \le f_{\mathrm{iden}} \le \omega_{os}/2/\pi$ is used in the identification stage, the identification result obtained is a unique solution. Therefore, the identification algorithm is simple and easy to implement;
2) Based on the developed WPT system prototype, the calculation process of the boundary conditions for load decoupling is explained in detail, and the sensitivity of the algorithm to the self-inductance parameters is analyzed as well. The conclusion is drawn that the identification accuracy can be effectively improved by using a smaller f_{iden} and self-inductance average correction.
3) Based on the theoretical analysis of the proposed method, a simulation model and experimental platform are developed. The results show that the mutual inductance identification method can effectively identify mutual inductance parameters with high accuracy. These works will lay a solid foundation for load identification, noncommunication control strategy and condition monitoring.

References

[1] K. Shuai *et al.*, "Modelling on mutual inductance of wireless power transfer for capsule endoscopy," *Biomed Microdevices*, vol. 22, no. 3, pp. 1–11, Aug. 2020.

[2] G. Xu *et al.*, "Design on magnetic coupling resonance wireless energy transmission and monitoring system for implanted devices," *IEEE Trans. Appl. Supercond* ., vol. 26, no. 4, Jun. 2016, Art. no. 4400804.

[3] M. A. Kirby *et al.*, "Wireless power and data transfer for electronic devices," U.S. Patent 12/614 272, Aug. 5, 2010.

[4] J. Zhou, B. Zhang, W. Xiao, D. Qiu, and Y. Chen, "Nonlinear parity-time-symmetric model for constant efficiency wireless power transfer: Application to a drone-in-flight wireless charging platform," *IEEE Trans. Ind. Electron.*, vol. 66, no. 5, pp. 4097–4107, May 2019.

[5] T. Kan, Y. Zhang, Z. Yan, P. P. Mercier, and C. C. Mi, "A rotation-resilient wireless charging system for lightweight autonomous underwater vehicles," *IEEE Trans. Veh. Technol.*, vol. 67, no. 8, pp. 6935–6945, Aug. 2018.

[6] X. Zhang, Z. Yuan, Q. Yang, Y. Li, J. Zhu, and Y. Li, "Coil design and efficiency analysis for dynamic wireless charging system for electric vehicles," *IEEE Trans. Magn.*, vol. 52, no. 7, Jul. 2016, Art. no. 8700404.

[7] D. S Manshadi, M. E. Khodayar, K. Abdelghany, and H. Üster, "Wireless charging of electric vehicles in electricity and transportation networks," *IEEE Trans. Smart Grid.*, vol. 9, no. 5, pp. 4503–4512, Sep. 2018.

[8] A. Ahmad, M. S. Alam, and R. Chabaan, "A comprehensive review of wireless charging technologies for electric vehicles," *IEEE Trans. Transp. Electrific.*, vol. 4, no. 1, pp. 38–63, Mar. 2018.

[9] K. N. Mude, "Battery charging method for electric vehicles: From wired to on-road wireless charging," *Chin. J. Elect. Eng.*, vol. 4, no. 4, pp. 1–15, Dec. 2018.

[10] A. Kumar, B. Regensburger, and K. K. Afridi, "A new design approach to mitigating the effect of parasitics in capacitive wireless power transfer systems for electric vehicle charging," *IEEE Trans. Transp. Electrific.*, vol. 5, no. 4, pp. 1040–1059, Dec. 2019.

[11] H. Zhou, A. Zhu, Q. Deng, J. Chen, F. Yang, and W. Hu, "Protection strategy for wireless charging electrical vehicles," *IEEE Trans. Veh. Technol.*, vol. 69, no. 11, pp. 13510–13520, Nov. 2020.

[12] D.-W. Seo, J.-H. Lee, and H.-S. Lee, "Optimal coupling to achieve maximum output power in a WPT system," *IEEE Trans. Power Electron.*, vol. 31, no. 6, pp. 3994–3998, Jun. 2016.

[13] B Zhang, Q. Chen, G. Ke, L. Xu, X. Ren, and Z. Zhang, "Coil positioning based on DC pre-excitation and magnetic sensing for wireless electric vehicle charging," *IEEE Trans. Ind. Electron.*, vol. 68, no. 5, pp. 3820–3830, May 2021.

[14] V. Jiwariyavej, T. Imura, and Y. Hori, "Coupling coefficients estimation of wireless power transfer system via magnetic resonance coupling using information from either side of the system," *IEEE J. Emerg. Sel. Topics Power Electron.*, vol. 3, no. 1, pp. 191–200, Mar. 2015.

[15] J. P. W. Chow, H. S.-H. Chung, and C.-S. Cheng, "Use of transmitter-side electrical information to estimate mutual inductance and regulate receiver-side power in wireless inductive link," *IEEE Trans. Power Electron.*, vol. 31, no. 9, pp. 6079–6091, Sep. 2016.

[16] J Yin, D. Lin, T. Parisini, and S. Y. Hui, "Front-end monitoring of the mutual inductance and load resistance in a series–series compensated wireless power transfer system," *IEEE Trans. Power Electron.*, vol. 31, no. 10, pp. 7339–7352, Oct. 2016.

[17] Y. Su, H.-Y. Zhang, Z.-H. Wang, A. P. Hu, L. Chen, and Y. Sun, "Steady-state load identification method of inductive power transfer system based on switching capacitors," *IEEE Trans. Power Electron.*, vol. 30, no. 11, pp. 6349–6355, Nov. 2015.

[18] Y. Su., L. Chen, X.-Y. Wu, A. P. Hu, C.-S. Tang, and X. Dai, "Load and mutual inductance identification from the primary side of inductive power transfer system with parallel-tuned secondary power pickup," *IEEE Trans. Power Electron.*, vol. 33, no. 11, pp. 9952–9962, Nov. 2018.

[19] L Chen *et al.*, "Load and mutual inductance identification method for series-parallel compensated IPT systems," *J. Power Electron.*, vol. 17, no. 6, pp. 1545–1552, Nov. 2017.

[20] Q Zhao, A. Wang, J. Liu, and X. Wang, "The load estimation and power tracking integrated control strategy for dual-sides controlled *LCC* compensated wireless charging system," *IEEE Access*, vol. 7, pp. 775749–775761, 2019.

[21] Y Yang, S. C. Tan, and S. Y. R. Hui, "Fast hardware approach to determining mutual coupling of series–series-compensated wireless power transfer systems with active rectifiers," *IEEE Trans. Power Electron.*, vol. 35, no. 10, pp. 11026–11038, Oct. 2020.

[22] W Shi, J. Deng, Z. Wang, and X. Cheng, "The start-up dynamic analysis and one cycle control-PD control combined strategy for primary-side controlled wireless power transfer system," *IEEE Access*, vol. 6, pp. 14439–14450, 2018.

[23] K. Hata, T. Imura, H. Fujimoto, and Y. Hori, "Soft-start control method for In-motion charging of electric vehicles based on transient analysis of wireless power transfer system," in *Proc. IEEE Energy Convers. Congr. Expo.*, 2018, pp. 2009–2015.

[24] D. S. Oliveira and I. Barbi, "A three-phase ZVS PWM DC/DC converter with asymmetrical duty cycle for high power applications," *IEEE Trans. Power Electron.*, vol. 20, no. 2, pp. 370–377, Mar. 2005.

[25] W Feng and F. C. Lee, "Optimal trajectory control of LLC resonant converters for soft start-up," *IEEE Trans. Power Electron.*, vol. 29, no. 3, pp. 1461–1468, Mar. 2013.
[26] R. Chang, B. Liu, and S. Duan, "Analysis and parameter optimization of start-up process for LLC resonant converter," *IEEE Trans. Power Electron.*, vol. 30, no. 12, pp. 7113–7122, Mar. 2015.
[27] A Nabih, M. H. Ahmed, Q. Li, and F. C. Lee, "Transient control and soft start-up for 1-MHz LLC converter with wide input voltage range using simplified optimal trajectory control," *IEEE J. Emerg. Sel. Topics Power Electron.*, vol. 9, no. 1, pp. 24–37, Feb. 2021.
[28] H Hu, T. Cai, S. Duan, X. Zhang, J. Niu, and H. Feng, "An optimal variable frequency phase shift control strategy for ZVS operation within wide power range in IPT systems," *IEEE Trans. Power Electron.*, vol. 35, no. 5, pp. 5517–5530, May 2019.
[29] M. Bojarski, E. Asa, K. Colak, and D. Czarkowski, "Analysis and control of multiphase inductively coupled resonant converter for wireless electric vehicle charger applications," *IEEE Trans. Transp. Electrific.*, vol. 3, no. 2, pp. 312–320, Jun. 2017.
[30] C. Riekerk *et al.*, "Study on soft start-up and shut-down methods for wireless power transfer systems for the charging of electric vehicles," in *Proc. IEEE PELS Workshop Emerg. Technol., Wireless Power Transf.*, 2021, pp. 1–6, doi: 10.1109/WoW51332.2021.9462867.
[31] D Patil, M. K. McDonough, J. M. Miller, B. Fahimi, and P. T. Balsara, "Wireless power transfer for vehicular applications: Overview and challenges," *IEEE Trans. Transp. Electrific.*, vol. 4, no. 1, pp. 3–37, Mar. 2018.
[32] F Liu *et al.*, "Research on the overall efficiency optimization of the bidirectional wireless power transfer system," *Trans. China Electrotech. Soc.*, vol. 34, no. 5, pp. 5–15, Mar. 2019.
[33] S. Z. Zhang, "Research on modeling and state estimation of vehicles LiFePO4 batteries," Ph.D. dissertation, Wuhan Univ. Technol., Wuhan, China, 2018.
[34] Z Wang *et al.*, "Research on protection circuit of power lithium batteries' charging and discharging," *Bus Coach Technol. Res.*, vol. 31, Aug. 2019, Art. no. 4.
[35] L Fang, "A selection method of mutual inductance identification models based on sensitivity analysis for wireless electric vehicles charging," in *Proc. IEEE Energy Convers. Congr. Expo.*, 2016, pp. 1–6.
[36] W. Li, J. Deng, T. D. Nguyen, and C. C. Mi, "A double-sided *LCC* compensation network and its tuning method for wireless power transfer," *IEEE Trans. Veh. Technol.*, vol. 64, no. 6, pp. 2261–2273, Jun. 2015.
[37] J. Acero, C. Carretero, I. Lope, R. Alonso, Ó. Lucia, and J. M. Burdio, "Analysis of the mutual inductance of planar-lumped inductive power transfer systems," *IEEE Trans. Ind. Electron.*, vol. 60, no. 1, pp. 410–420, Jan. 2013.
[38] D.-H. Kim and D. Ahn, "Self-tuning *LCC* inverter using PWM-controlled switched capacitor for inductive wireless power transfer," *IEEE Trans. Ind. Electron.*, vol. 66, no. 5, pp. 3983–3992, May 2019.
[39] Y Guo, Y. Zhang, S. Li, C. Tao, and L. Wang, "Load parameter joint identification of wireless power transfer system based on the DC input current and phase-shift angle," *IEEE Trans. Power Electron.*, vol. 35, no. 10, pp. 10542–10553, Oct. 2020.

Lei Wang received the M.S. degree in instrument science and technology from Southwest Petroleum University, Chengdu, China, in 2016. She is currently working toward the Ph.D. degree with the Naval University of Engineering, Wuhan, China.

Her research interests include circuit topology, analysis, and parameter identification of wireless power transfer.

Pan Sun received the B.S. degree in electrical engineering and automation, and the M.S. degree in electrical engineering from the Naval University of Engineering, Wuhan, China, in 2009 and 2015, respectively.

In June 2015, he joined the College of Electrical Engineering, Naval University of Engineering, as a Lecturer. His research interests include wireless power transfer, design, and verification of testability.

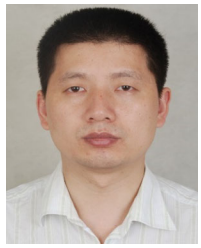

Xusheng Wu received the B.S., M.S. Tech., and Ph.D. degrees from the College of Electrical and Informational Engineering, Naval University of Engineering, Wuhan, China, in 1996, 1999, and 2004, respectively.

He is currently a Professor with the College of Electrical and Informational Engineering, Naval University of Engineering. His research interests include wireless power transfer, electric devices, and power systems on warships.

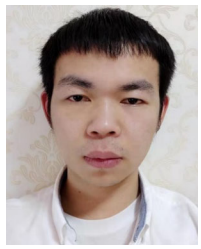

Jin Cai received the M.Sc. degree from the National University of Defense Technology, Changsha, China, in 2015. He is currently working toward the Ph.D. degree with the Naval University of Engineering, Wuhan, China.

His current research interests include wireless power transfer.

Qijun Deng received the B.S. and M.Sc. degrees in mechanical engineering and the Ph.D. degree in computer application technology from Wuhan University, Wuhan, China, in 1999, 2002, and 2005, respectively.

In June 2005, he joined the Department of Automation (which is now merged with the School of Electrical Engineering and Automation), Wuhan University, where he is currently a Professor. From 2013 to 2014, he was a Visiting Scholar with New York University Tandon School of Engineering, Brooklyn, NY, USA. His research interests include wireless power transfer, distribution automation, and electrical power informatic.

Jun Sun received the M.S. degree in electrical engineering from the Naval University of Engineering, Wuhan, China, in 2017.

He is currently a Teaching Assistant with the Naval University of Engineering. His research interests include high-efficiency power conversion technology and high-power wireless power transfer technology.

Hang Zhou received the B.S. and Ph.D. degrees from Wuhan University, Wuhan, China, in 2016 and 2021, respectively, both in electrical engineering.

He is currently a Lecturer with the College of Electrical and Engineering, Naval University of Engineering, Wuhan, China. His research interests include fault current limiters in HVdc system and wireless power transfer.